Originally published as:

Monitoring of saturation changes and salt precipitation during CO₂ injection using pulsed neutron-gamma logging at the Ketzin pilot site

Authors: G. Baumann, J. Henninges, M. De Lucia

Gunther Baumann
German Research Centre for Geosciences GFZ
Tel: +49 (0) 331 288 1970
Fax: +49 (0) 331 288 1577
baumann@gfz-potsdam.de

Jan Henninges
German Research Centre for Geosciences GFZ
Tel: +49 (0) 331 288 1442
janhen@gfz-potsdam.de

Marco De Lucia
German Research Centre for Geosciences GFZ
Tel: +49 (0) 331 288 2829
delucia@gfz-potsdam.de

Abstract

During injection of CO_2, monitoring of the subsurface saturation changes is required. For well logging in cased boreholes only a limited number of techniques such as radiometric pulsed neutron-gamma (PNG) logging are applicable. The conventional PNG saturation model mainly considers a displacement process. But during CO_2 injection additional processes such as evaporation and salt precipitation are expected to occur as a result of the mutual solubility between brine and CO_2. For this purpose an extended PNG saturation model for NaCl-brines is developed and applied to a time-lapse PNG monitoring data set from the Ketzin site. The results show that for the observation well further away from the injection well, the conventional displacement saturation model is valid, with average CO_2 saturations below 60 %. In contrast, the data from the injection well shows that both evaporation and salt precipitation have occurred. Here, the largest CO_2 saturations with values up to 100 % are determined locally. The results of the extended saturation model indicate that dry-out regions, where only CO_2 and halite with saturations up to 1.4 % exist, and maximum halite saturations up to 14.1 % occur in the vicinity of the brine levels. The halite saturation distribution in the injection well seems to be controlled by changes in the injection regime associated with changing brine levels, lithological heterogeneities, and capillary effects. PNG monitoring in combination with the extended saturation model is suited to determine displacement and evaporation/precipitation processes for CO_2 storage operations.

Keywords: CO2 storage, pulsed neutron-gamma, displacement, evaporation, salt precipitation, Ketzin

1. Introduction

The storage of carbon dioxide (CO_2) in geological formations is currently discussed as a possible option to reduce emissions of greenhouse gases to the atmosphere. During the proposed CO_2 injection process, application of suitable techniques for monitoring of the induced changes in the subsurface is required. Existing reservoir models for the spreading of the CO_2, as well as displacement processes or resulting issues from mutual solubility between brine and CO_2 associated with saturation changes, need to be checked.

Different mechanisms can lead to saturation changes in the proximity of an injection well. First, the injected dry CO_2 displaces the mobile brine. Additionally, H_2O is vaporized or dissolved into the CO_2-rich phase. The removed liquid H_2O component causes therefore an increase in brine salinity. Upon reaching the solubility limit, removing additional H_2O leads to salt precipitation. Evaporation and precipitation processes are of practical relevance in the vicinity of gas production and injection wells, where complete blockage of flow paths can occur (Kleinitz et al., 2003). Modeling results show that gravity-forced upflow of CO_2 and capillary-forced backflow of brine toward the injection point can enhance salt precipitation (e.g. Pruess and Müller 2009).

The conventional PNG saturation model mainly considers displacement and has been successfully used for PNG interpretation in different CO_2 storage projects in saline aquifers (Frio: Sakurai et al., 2005; Müller et al., 2007. Nagaoka: Xue et al. 2006; Murray et al., 2010). The main PNG derived parameters are the macroscopic capture cross section (Σ) and the neutron porosity (TPHI) of the formation. The high measurement contrast between brine and CO_2 results in a high sensitivity to evaluate saturation changes. The conventional displacement saturation model accounts for mixing of the fluids in the pore space but ignores evaporation and precipitation processes. However, since the Σ brine value (Σ_{br}) strongly depends on the brine salinity, e.g. its chlorine content, PNG measurements are sensitive for the effects resulting from evaporation and salt precipitation (Baumann and Henninges, 2012). For this purpose an extended PNG saturation model for NaCl-brines including both displacement and evaporation/precipitation processes was developed (Section 4.2) and applied to the PNG monitoring data at the Ketzin pilot site (Section 5).

The general objective at the Ketzin pilot site is to understand in situ ongoing processes associated with geological storage of CO_2 in a saline aquifer (Würdemann et al., 2010; Martens et al., 2012, 2013). For this purpose, an extensive monitoring program is performed (Giese et al., 2009), including different geophysical techniques, which cover the large "reservoir scale" associated with a low spatial resolution. In contrast to these methods, PNG logging covers the small "borehole scale", with a corresponding high spatial resolution. Based on an integrated evaluation of these different monitoring techniques, with their variability in scale and spatial resolution, the spreading of the CO_2 is mapped (e.g. Ivanova et al., 2012; Bergmann et al., 2012). Thereby, PNG-derived CO_2 saturations in the injection and observation wells are used as input parameters for the seismic and electric interpretations.

The Ketzin pilot site is located approximately 25 km west of Berlin, in the eastern part of the Roskow-Ketzin double anticline. Three vertical wells were drilled into the flank of the anticline in 2007, i.e. one injection well (Ktzi 201) and two observation wells (Ktzi 200 and Ktzi 202). Ktzi 200 is about 50 m and Ktzi 202 is about 112 m from the injection well. In summer 2011, the shallow vertical observation well P300 penetrating the first aquifer above the injection reservoir, and in summer 2012 the vertical

observation well Ktzi 203 were drilled (Figure 1). Wells Ktzi 200, Ktzi 201 and Ktzi 202 are the focus for the presented PNG monitoring results, since it is mainly in these wells that the extensive PNG monitoring was conducted.

2. Ketzin pilot site geology, injection history and well completions
2.1. Geology

The injection reservoir is the Upper Triassic Stuttgart formation. The heterogeneous lithology of the Stuttgart formation is associated with a heterogeneous porosity and permeability distribution (Förster et al., 2010). The main reservoir sandstone unit (634-651 m) of the Stuttgart formation in Ktzi 201 and Ktzi 200 is subdivided into two permeable sandstone layers, which are separated by an interbedded strongly cemented sandstone layer. Both sandstone layers have a relatively high clay content associated with high irreducible brine saturation (S_{br-irr}) (Kummerow and Spangenberg, 2011). In Ktzi 201, a second permeable interval below the main reservoir sandstones is present at a depth of 651-664 m, which is comprised of silt- and sandstones. According to the position within the anticline, the main reservoir sandstone in Ktzi 202 is shallower (627-638 m) and thinner, and especially the lower part has higher clay content with less porosity and permeability than in Ktzi 200 or Ktzi 201 (Norden et al., 2010). The overlaying seal of the Stuttgart formation is the Weser formation, which is characterized by mudstones, clayey siltstones, anhydrite and dolomite (Förster et al., 2010; Norden et al., 2010).

2.2. Injection history

Figure 2 shows a temporal overview of the different PNG logging runs together with the injection history between June 2008 and August 2013. From June 2008 until March 2009, the injection rate was gradually increased to a maximum of 3.5 t/h, and then proceeded at this rate for a period of around one year (March 2009 until March 2010). From March 2010 until May 2012, the injection rate was roughly halved, with short periods of an increased injection rate. Between May 2012 and January 2013 a shut-in period commenced. Mid of January 2013 injection is resumed and proceeded until injection was finally completed in August 2013. These changing injection rates are associated with changing brine level within the wells (Table 3). The total injected CO_2 mass is about 67,000 t.

2.3. Well completions

The reservoir section was drilled with 8.5 inch bit size and completed with a 5.5 inch plastic coated steel production casing, with a casing weight of 20 lb/ft.
Due to the smart casing concept, that uses different sensor cables and installations behind casing for monitoring, the production casings are partially not cemented. This is the case in Ktzi 201 (for details, see Prevedel et al., 2008) and Ktzi 202, where the upper cemented interval of the 5.5 casing annulus starts about 50 m above the reservoir interval at the level of the following 9-5/8 inch casing. In contrast, only the annulus in Ktzi 200 (Figure 7) is cemented in the interval immediately above the reservoir section. The wells are hydraulically connected with the reservoir using pre-installed filter screens (Prevedel et al., 2008).

The open or partly cemented annuli in the reservoir section are associated with changing borehole conditions, because fluids in both the boreholes and the annuli change during CO_2

3

injection. These changing borehole conditions between baseline and repeat runs must be carefully taken into account when characterizing the saturation changes in the reservoir. This is discussed in Section 3.2.

3. Fluid Σ, HI values and PNG data processing

3.1. Fluid Σ and HI values

Similar to many brines from the North German Basin at corresponding depth (Tesmer et al., 2007), the Ketzin brine is dominated by NaCl. This allows for a common assumption made in PNG interpretation (e.g. Serra, 1984), which is considering all dissolved salts by a NaCl-equivalent concentration ($c_{NaCl-eq}$). Such equivalent concentration was chosen in order to preserve the same PNG signal as the actual Ketzin brine's chemical analysis after Würdemann et al. (2010). Under this assumption, $c_{NaCl-eq}$ is 220 g/l under Ketzin reservoir conditions (35 °C, 7.5 MPa). The concentration of the liquid water component of the brine, c_{H2O}, is then calculated as the difference between the mass of 1 liter of solution (brine density ρ_{br} times 1000) and the total amount of dissolved solids per liter of solution, which in this case is just the $c_{NaCl-eq}$. ρ_{br} is 1.14 g/cm³ calculated after Rowe und Chou (1970) at 35 °C and 7.5 MPa.

The Σ brine value (Σ_{br}) can be calculated from a chemical analysis (Serra, 1984). Thus, Σ_{br} for a NaCl-brine results from the sum of the capture cross sections of the solvent water (Σ_{H2O-c}) and the dissolved NaCl (Σ_{NaCl-c}), which are calculated from the NaCl ($c_{NaCl-eq}$) and water (c_{H2O}) concentrations in g/l brine and the corresponding mass-normalized microscopic capture cross sections (σ_{m-NaCl} and σ_{m-H2O}) in cm²/g.

$$\Sigma_{br} = \Sigma_{H2O-c} + \Sigma_{NaCl-c} = c_{H2O} \cdot \sigma_{m-H2O} + c_{NaCl-eq} \cdot \sigma_{m-NaCl} \text{ (Eq. 1)}$$

The mass-normalized microscopic capture cross sections are calculated using the element specific capture cross sections from Sears (1992), the atomic mass from Afeefy et al. (2005) and Avogadro's number. Overall, Σ_{NaCl-c} is 77.15 cu and Σ_{H2O-c} is 22.43 cu, which results in a Σ_{br} value of 97.58 cu under Ketzin reservoir conditions. The Σ_{CO2} value for the Ketzin reservoir conditions results in 0.014 cu. Table 1 summarizes the calculated fluid Σ values and Table 4 the used abbreviations.

The hydrogen index (HI) values of the fluids are input parameters to derive the saturation conditions from the neutron porosity (TPHI). The HI of the Ketzin brine (HI_{br}=0.92) is calculated after Ellis et al. (1987) based on Σ_{br}. Since CO_2 and NaCl contain no hydrogen, the HI for CO_2 and NaCl is zero.

3.2. PNG data processing

Table 2 and Figure 2 show the dates when the PNG logging runs were carried out in Ktzi 200, Ktzi 201 and Ktzi 202 using the Schlumberger Reservoir Saturation Tool (RST). The baseline runs were performed two weeks before CO_2 injection started on June 24th, 2008. On June 19th, 2008, about one week after the baseline runs had been carried out, a low-salinity KCl-preflush was performed in Ktzi 201 in order to reduce the formation brine salinity and reduce the risk of halite scaling in the vicinity of the injection well (Würdemann et al., 2010). In order to account for the related change in Σ and TPHI, synthetic baseline logs are developed (see Section 0).

During the injection period six repeat logging runs were performed in about annual intervals. The first repeat was only performed in Ktzi 200, immediately after the arrival of CO_2 was observed at this observation well using a downhole gas membrane sensor in July 2008 (Zimmer et al., 2011), whereas the subsequent repeat runs were performed in all wells respectively.

RST data processing involves transfer of apparent into true or intrinsic quantities using environmental corrections, for which borehole and completion data are required as input parameters (Plasek et al., 1995). In the following the main processing parameters are described.

For both the baseline and repeat run data, constant well completion parameters according to the 5.5" section of the wells (8.5" bit size, 5.5" casing size and 20 lb/ft casing weight, see Section 2.3) have been used, and the matrix rock type was set to sandstone. When the well is filled with brine, the salinity of the borehole fluid is preset to a value of 197 ppk, which corresponds to a salinity similar to the formation brine (see Section 3.1). This applies to the baseline runs, the repeat 1 in Ktzi 200, and to the well sections below the brine level of the following repeats.

In contrast to the baseline runs, the repeat runs are characterized by changing brine levels in the boreholes. It should be noted that we will use throughout the paper the term "brine level" referring to the water level within the well, which is not necessarily similar to the level of the gas-water contact (usually named GWC) inside the formation. For the repeat runs above the brine level, the borehole and sections of the annuli are filled with CO_2, which is taken into account by setting the borehole status to "air". The positions of the brine levels could be determined from the logging data itself and are listed in Table 3.

The RST processing algorithm nevertheless assumes cemented annuli, where no fluid exchange can occur (Plasek et al., 1995). Thus, the borehole status "air" accounts for the borehole effect from the CO_2 within the well, but not for the borehole effect resulting from the CO_2 in uncemented annuli.

The CO_2 in the uncemented annuli mainly affects TPHI, which is derived from near and far detectors, whereas formation Σ is derived from the far detector only (Plasek et al., 1995). Nevertheless, TPHI is an input parameter for computation of the Σ values (Eqs. (4) and (5) in Plasek et al., 1995). To account for these short-comings, the total porosity derived from the open hole logging data (Norden et al., 2010) was additionally used as external knowledge for processing of the repeat Σ curves, which is equivalent to the approach applied by Müller et al. (2007) for processing of a similar time-lapse RST data set from the Frio project. For the repeat runs TPHI data processing the standard processing using the borehole status "air" is used.

4. Conventional versus extended PNG saturation model

4.1. Conventional saturation model

The conventional model accounts for mixing of the fluids in the pore space but ignores any mutual physico-chemical interaction (Figure 3). The formation Σ value (Σ_{tot}) results from the individual volume fractions i of the matrix, the fluid filled pore space and their corresponding Σ_i values (e.g. Serra 1984). Thus, the conventional displacement baseline model (Σ_B) before injection results in:

$$\Sigma_B = \left(1 - \Phi_{tot}\right) \cdot \Sigma_{ma} + \Phi_{tot} \cdot \Sigma_{br} \quad \text{(Eq. 2)}$$

while the repeat model (Σ_R) is:

$$\Sigma_R = \left(1 - \Phi_{tot}\right) \cdot \Sigma_{ma} + \Phi_{tot} \cdot \left(S_{br} \cdot \Sigma_{br} + S_{CO2} \cdot \Sigma_{CO2}\right) \quad \text{(Eq. 3)}$$

where Φ_{tot} is the total porosity, and the subscripts ma, br and CO_2 correspond to the matrix, brine and CO_2 components respectively. Thereby, the CO_2 saturation S_{CO2} (referred to the total porosity Φ_{tot}) can be directly calculated from the difference between Eqs. (2) and (3).

$$S_{CO2} = 1 - S_{br} = \frac{\Sigma_B - \Sigma_R}{\Phi_{tot} \cdot \left(\Sigma_{br} - \Sigma_{CO2}\right)} \quad \text{(Eq. 4)}$$

4.2. Extended saturation model

The proposed extended PNG saturation model aims at including both the displacement and evaporation/precipitation processes by discriminating in greater detail the proportions of pore space occupied by the different phases (brine, gas, precipitated salt), hence explicitly accounting for possible increase of salt load in the proximity of the boreholes. It needs to be stressed out, however, that this model, just as the conventional, is merely descriptive and aimed at the interpretation of the PNG readings and not at the quantification of the underlying ongoing physical processes.

The total porosity Φ_{tot} can be divided into two fractions, initially occupied by a mobile (Φ_{eff}) and an immobile (Φ_{irr}) phase (Figure 4), where Φ_{irr} ($\Phi_{irr} = S_{br-irr} \cdot \Phi_{tot}$) is defined by the irreducible brine saturation (S_{br-irr}). Similarly, the total CO_2 saturation S_{CO2}, results from the volume weighted sum of the individual CO_2 saturations $S_{CO2-eff}$ and $S_{CO2-irr}$ related to Φ_{eff} and Φ_{irr}, respectively. One underlying simplification in the proposed model is that the brine's mobile fraction be completely displaced by CO_2 before any relevant evaporation/precipitation process initiates in the pore volume. Thus, evaporation of H_2O and therefore salt precipitation is considered to affect only the pore volume fraction occupied by the irreducible brine saturation. This simplification appears justified since, given the order of magnitudes of mutual solubility of water and CO_2 (e.g. Spycher et al., 2003), only a few dozens pore volume cycles of flooding CO_2 are sufficient to nearly reach irreducible water saturation of an initially brine-saturated pore volume, whereas several hundreds cycles are needed for the brine to reach salt solubility limit and thus initiate significant salt precipitation. Accordingly to this consideration, first the mobile brine (Φ_{eff})

is displaced and subsequently the immobile water fraction (Φ_{irr}) begins evaporating by CO_2 (Figure 4).

The evaporation/precipitation part of the extended saturation model considers explicitly water and NaCl volume fractions in brine (Figure 4, Φ_{irr}). These volume fractions or saturations in brine, S_{NaCl-B} and S_{H2O-B}, are apparent values, because the respective components are contained within the brine in solution, as opposed to separate volume fractions. It is important to point out that, concerning the PNG reading, it is irrelevant whether the NaCl is dissolved in brine or precipitated as halite: the original NaCl content remains unchanged in Φ_{irr}, since only the H_2O component of the immobile brine gets removed upon evaporation. The volume fraction occupied by precipitated halite after complete evaporation of water ($S_{NaCl-pre}$, Figure 4) can be calculated directly from the initial NaCl concentration in the brine, $c_{NaCl-eq}$, and halite density (ρ_{NaCl}=2.165 g/cm³, e.g. Serra, 1984). Therefore, as an extension to Eq. (1), the apparent saturations S_{NaCl-B} and S_{H2O-B}, in combination with the halite and water Σ values (Σ_{NaCl}=760.9 cu and Σ_{H2O-br}), can be used to describe Σ_{br}:

$$\begin{aligned} \Sigma_{br} &= S_{H2O-B} \cdot \Sigma_{H2O-br} + S_{NaCl-B} \cdot \Sigma_{NaCl} \\ &= 1000 \cdot \left(S_{H2O-B} \cdot \sigma_{m-H2O} \cdot \rho_{H2O-br} + S_{NaCl-B} \cdot \sigma_{m-NaCl} \cdot \rho_{NaCl} \right) \end{aligned} \quad \text{(Eq. 5)}$$

The subscript "B" in S_{NaCl-B} and S_{H2O-B} indicates that this is the baseline or initial condition for the evaporation/precipitation model. The subscript "br" in Σ_{H2O-br} and ρ_{H2O-br} specifies the relation to brine. As evident from Figure 4, a closure equation can be written for this binary system, ensuring that the sum of S_{NaCl-B} and S_{H2O-B} is initially equal to one. For the Ketzin brine under reservoir conditions S_{NaCl-B} is 0.10 and S_{H2O-B} is 0.90. Based on the brine density and closure equation, an auxiliary water density in brine (ρ_{H2O-br}) can be calculated. ρ_{H2O-br} is equal to pure water density for c_{NaCl}=0 and increases slightly with increasing salinity. This increase is due to the volume change upon mixing where H_2O and NaCl in solution occupy a smaller volume than the sum of the separate components (pp 32-37 in Baumann, 2013). However, within the typical PNG tools precision (0.22 cu; Plasek et al., 1995) for the Ketzin reservoir conditions, it is safe to neglect such non linear density behavior (pp 44-49 in Baumann, 2013).

Furthermore, the CO_2 component in the aqueous phase and the H_2O component in the CO_2-rich phase (Spycher et. al., 2003; Spycher and Pruess, 2005) can be neglected within the typical precision of PNG tools (pp 30-31 in Baumann, 2013). Pressure and temperature correspond to the initial reservoir conditions (35 °C and 7.5 MPa) and are assumed to be constant throughout. Similarly it is assumed that the rock matrix is non-reactive at least at the time-scale of injection operations and thus constant.

In contrast to the conventional baseline model, the extended one includes the water fraction $S_{H2O-B}\Sigma_{H2O-br}$ and dissolved salt fraction $S_{NaCl-B}\Sigma_{NaCl}$ in Φ_{irr}. Both the conventional and extended models result in the same Σ_B value. Here, the saturation based Σ_{br} declaration is used to apply the evaporation/precipitation model on the Σ fractions corresponding to Φ_{irr}. Summing up, the baseline Σ_B in the extended saturation model can be written as:

$$\Sigma_B = \left(1 - \Phi_{tot}\right) \cdot \Sigma_{ma} + \Phi_{eff} \cdot \Sigma_{br} + \Phi_{irr} \cdot \left(S_{H2O-B} \cdot \Sigma_{H2O-br} + S_{NaCl-B} \cdot \Sigma_{NaCl}\right)$$
$$= \Sigma_{B-ma} + \Sigma_{B-eff} + \Sigma_{B-irr}$$
(Eq. 6)

The H_2O evaporation from the liquid phase results in an additional volume fraction occupied by CO_2 in Φ_{irr}. The Σ value for NaCl saturated brine, Σ_{br-lim}, (assuming halite solubility, 266 ppk, following Potter et al., 1977) is 131.2 cu for the Ketzin site reservoir conditions. The corresponding $S_{NaCl-lim}$ value at the halite solubility limit is 0.15 and the $S_{H2O-lim}$ value is 0.85, which are used as criterion for initiating precipitation.

During evaporation, the transfer from dissolved to precipitated NaCl is controlled by the remaining water saturation (S_{H2O-R}) that decreases with increasing CO_2 saturation ($S_{CO2-irr}$) in Φ_{irr}. Finally, when all water is evaporated the precipitated halite saturation $S_{NaCl-pre}$ is equal to the initial dissolved NaCl saturation $S_{NaCl-sol}$ (Figure 4, ϕ_{irr}).

Therefore, the extended repeat model includes the CO_2 fraction $S_{CO2-irr}\Sigma_{CO2}$, the remaining water fraction $S_{H2O-R}\Sigma_{H2O-br}$ and the dissolved or precipitated salt fractions ($S_{NaCl-sol}+S_{NaCl-pre}$)$\Sigma_{NaCl}$ in Φ_{irr}.

$$\Sigma_R = \left(1 - \Phi_{tot}\right) \cdot \Sigma_{ma} + \Phi_{eff} \cdot \left[S_{br-eff} \cdot \Sigma_{br} + \left(1 - S_{br-eff}\right) \cdot \Sigma_{CO2}\right]$$
$$+ \Phi_{irr} \cdot \left[S_{H2O-R} \cdot \Sigma_{H2O-br} + \left(S_{NaCl-sol} + S_{NaCl-pre}\right) \cdot \Sigma_{NaCl} + \left(S_{H2O-B} - S_{H2O-R}\right) \cdot \Sigma_{CO2}\right] \text{(Eq. 7)}$$
$$= \Sigma_{R-ma} + \Sigma_{R-eff} + \Sigma_{R-irr}$$

The system in Φ_{irr} is constraint by the following conditions:

$$S_{H2O-R} + S_{CO2-irr} + S_{NaCl-sol} + S_{NaCl-pre} = 1 \text{(Eq. 8)}$$

$$S_{CO2-irr} = S_{H2O-B} - S_{H2O-R} \text{ (Eq. 9)}$$

$$S_{NaCl-B} = S_{NaCl-sol} + S_{NaCl-pre} \text{(Eq. 10)}$$

The extended saturation model is further divided into two cases. If $\Sigma_R \leq \Sigma_B$, first the displacement saturation model and subsequently the evaporation/precipitation saturation model are applied. Both saturation mechanisms result in a decreased Σ value compared to the baseline run. If $\Sigma_R > \Sigma_B$, the pore fluid Σ value is increased which can be interpreted as an increase in salt load. Thus, Σ_{R-ma} (Eq. (7)) is equal to Σ_{B-ma} (Eq. (6)) and is calculated from the baseline Σ run and the known Σ_{br} and Φ_{tot} values. Σ_{B-eff} and Σ_{B-irr} result from Σ_{br} and Φ_{eff} or Φ_{irr}, respectively. Table 4 summarizes the used abbreviations for the conventional and extended saturation model. Details of both cases are described in the following sections.

4.2.1. $\Sigma_R \leq \Sigma_B$: displacement and subsequent evaporation/precipitation model

$S_{CO2-eff}$ is obtained from equation 4 with Φ_{eff} as porosity input. As long as $S_{CO2-eff}$ is smaller or equal to one, only displacement takes place. With onset of evaporation/precipitation, $S_{CO2-eff}$ is limited to a value of one. Therefore, a further Σ decrease can only result from

evaporation/precipitation in Φ_{irr}. The saturation conditions pertaining to Φ_{irr} in Eq. (7) are calculated from the resulting Σ difference ($\Sigma_{B\text{-}irr}$-$\Sigma_{R\text{-}irr}$) between the calculated and the measured Σ_R values. Thereby, the whole evaporation/precipitation process is reduced to one unknown saturation $S_{CO2\text{-}irr}$, since $S_{H2O\text{-}R}$ results directly from $S_{CO2\text{-}irr}$. The interpretation here is that the initial NaCl load remains constant and is just transferred from solution to precipitants between the runs. If the minimum possible Σ_R value is reached after complete evaporation ($S_{H2O\text{-}r}$=0, $S_{NaCl\text{-}pre}$=$S_{NaCl\text{-}B}$, $S_{CO2\text{-}irr}$=1-$S_{NaCl\text{-}pre}$), and the calculated Σ_R value is still greater than the measured one, Φ_{eff} (increased) and Φ_{irr} (decreased) are adjusted within the limit of ϕ_{tot}.

4.2.2. $\Sigma_R > \Sigma_B$: increased overall Σ pore fluid value

An increased Σ reading with respect to baseline points out an increase of salt load in the pore volume, either in form of solutes, precipitates, or a combination of both. A possible physical explanation for such an increase is counter imbibition of formation brine, coupled with evaporation, salting up and precipitation. Counter imbibition can result from the presence of local reservoir heterogeneities, namely, preferential flow paths and capillary forces recalling brine from contiguous pore volumes. This additional brine supply in turn enables further precipitation of salt until clogging is reached and the local loss of injectivity cancels out the preferential flow paths. This combination of processes is also predicted to occur by numerical models (e.g. Pruess & Müller, 2009).

In the abstraction adopted for the extended saturation model, a precondition for evaporation is that the mobile brine is completely displaced and $S_{CO2\text{-}eff}$ is one. If a back flow rate of brine equal to the evaporation rate is assumed, $S_{CO2\text{-}irr}$ is zero, because the developing "free" volume fraction from water evaporation is directly occupied by the back flowing brine. The salinity and hence the Σ value of the remaining brine in Φ_{irr} would increase continuously, because the water lost by evaporation is replaced by saline formation brine with a higher Σ value. Assuming a diffusion driven salinity equilibration during this process between the back flowed brine and the remaining high salinity brine, the overall brine salinity increases. Reaching the NaCl solubility limit, halite precipitation occurs. After further counter imbibitions of brine, Φ_{irr} can finally become completely clogged by halite. So Eq. (7) for the extended saturation repeat model can be rewritten for $S_{br\text{-}eff}$=0 and using a remaining Σ_x value representing Φ_{irr}.

$$\Sigma_R = \Sigma_{R-ma} + \Phi_{eff} \cdot \Sigma_{CO2} + \Phi_{irr} \cdot \Sigma_x \quad \text{(Eq. 12)}$$

After application of Eq. (12), the brine and salt saturations in Φ_{irr} are derived from Σ_x using the Σ values for either brine with increased salinity, NaCl saturated brine ($\Sigma_{br\text{-}lim}$) and/or halite (Σ_{NaCl}).

Based on evidence from the Ketzin PNG logging data, it was necessary to develop an alternative approach, avoiding the model assumption that $S_{CO2\text{-}eff}$ is one and $S_{CO2\text{-}irr}$ is zero. As will be seen in Section 5, several depth intervals where the $\Sigma_R > \Sigma_B$ case applies are characterized by rather high TPHI readings. These high TPHI readings indicate the presence of

9

larger quantities of brine, thus lower CO_2 saturations compared to the model assumption that $S_{CO2-eff}$ is one and $S_{CO2-irr}$ is zero. In the concerned intervals the total CO_2 saturation, S_{CO2}, is derived from the neutron porosity, in analogy to Eq. (4), with the baseline and repeat TPHI values, and HI values for brine and CO_2 as input parameters (see Section 3.1). As before, a remaining Σ_x value is calculated in order to account for the increasing salinity due to capillary effects.

5. PNG monitoring results at the Ketzin site

The saturation profiles for all wells are calculated using both the conventional as well as the extended saturation model approaches described above. The main input parameters are the differences between the baseline and repeat Σ logs (see Section 3.2), the calculated Ketzin fluid Σ values (see section 3.1) and the Φ_{eff} and Φ_{tot} logs derived from the open-hole logging data (Norden et al., 2010).

For the processing of the PNG data, the brine level during each run was extracted from the PNG and pressure-temperature logging data (Table 3). The position of the interface between brine and CO_2 was determined from the resulting change of the measured apparent Σ and the density of the borehole fluid.

The positions of the brine levels within the wells generally depend on the injection regime. During the baseline runs before the start of injection, the brine level was at a depth of about 100 m in all wells. After start of injection and arrival of CO_2, the wells began to gradually fill up with CO_2, pushing the brine levels to successively greater depths. The first repeat in Ktzi 200 was run immediately after the arrival of the CO_2, and the brine level had dropped to 206.35 m, still far above the reservoir. The deepest brine levels are determined at around 650 m and occur during the time of the highest injection rates, i.e. during the second repeat in Ktzi 201 and Ktzi 200 and the third repeat in Ktzi 202. Afterwards, the brine levels are rising again in all wells, which corresponds to the decrease in injection rate during the subsequent repeats. The increase of the brine level after the fourth repeat in Ktzi 200 is much larger than within the other wells, and was most likely caused by a withdrawal of fluid from the well during fluid sampling. In general, the shallowest brine levels appear during the sixth repeat, after injection had been shut-in for a period of six months.

In the following sections, the results for the conventional and the extended saturation models are described. In Table 5, average calculated CO_2 saturations for the main porous and permeable reservoir sections of the different wells are listed.

5.1. Conventional saturation model

The saturation calculations for the conventional saturation model are performed according to Eq. (4) using the measured baseline Σ logs.

5.1.1. Injection well Ktzi 201

In Fig. 5 the measured PNG data and the calculated saturation profiles for the Ktzi 201 injection well are displayed. CO_2 (S_{CO2} in green) and accordingly brine (S_{br} in blue) are shown as fractions of Φ_{tot} for each repeat run. The white logs shown in each saturation profile

separate the pore volume fractions occupied by mobile (Φ_{eff}/Φ_{tot}) and immobile (Φ_{irr}/Φ_{tot}) brine. A S_{CO2} value greater than Φ_{eff}/Φ_{tot} suggests that, in addition to displacement, evaporation is occurring. This "apparent" S_{CO2} fraction, which cannot be displaced, is therefore shown in light green.

As expected, the Σ repeat logs (Fig. 5, track v) decrease compared to the baseline logs in the main reservoir sandstone, which is characteristic for all wells. In general, similar changes in the repeat Σ and TPHI logs can be observed (Fig. 5, track iv), and a decreased Σ reading corresponds to a decreased TPHI reading.

Except in the lower most part, all repeat Σ and TPHI logs nearly overlap in the upper sandstone layer, resulting in almost constant saturation conditions over time within this interval. In the middle part, the highest S_{CO2} occur, with values up to 100 % locally. Increases above the mobile brine fraction indicate that the displacement model is not sufficient for a consistent explanation of the measured data in the concerned intervals. During the sixth repeat, the Σ and TPHI logs again increase in the lower most part of the upper sandstone layer. The resulting decrease in CO_2 saturation correlates with a rise of the brine level between the fifth and the sixth repeat.

In the lower sandstone layer, the repeat Σ and TPHI logs reach their minimum for the second repeat and then increase for all subsequent repeats. S_{CO2} is maximal in the upper part, again exceeding the mobile brine fraction, and decreases with increasing depth. Between 645 and 648 m, the fourth and the fifth repeat Σ logs are characterized by prominent peaks that are greater than the baseline log. The displacement saturation model is again not able to account for these elevated repeat Σ values, which would result in negative CO_2 saturations using Eq. (4). S_{CO2} was therefore set to zero in the concerned intervals for the fourth and fifth repeats (see Section 4.1).

Further below, in the silt- and sandstone layer between 651 and 664 m, the second and the third repeat Σ and TPHI logs have slightly lower readings than the baseline logs, resulting in average CO_2 saturations between 12 % and 21 %. In contrast, all subsequent repeats nearly overlap with the baseline logs indicating a decrease of CO_2 saturation, which corresponds to the decreased injection rate after March 2010.

Above the reservoir interval, an offset between the baseline and repeat Σ and TPHI logs is visible as a result of the gas-filled annulus (see Sections 2.2 and 3.2). Affected depth intervals are located above the injection horizon in all wells, but also occur below the main reservoir intervals (cf. results for Ktzi 202 described below).

5.1.2. Observation well Ktzi 200

In the upper sandstone layer, a general decrease of Σ and TPHI from the first up to the fourth repeat can be observed (Fig. 6). The maximum S_{CO2} calculated for the first repeat is 53 %, and S_{CO2} then increases during the subsequent repeat runs, especially in the middle part of the upper sandstone layer. After the second repeat, the logs nearly overlap in the middle part of the upper sandstone layer, indicating only minor changes between these runs within this

interval. The shape of the CO_2 saturation profile is therefore similar for the second, third and fourth repeats, where a maximum S_{CO2} of 91 % is calculated. S_{CO2} is partly exceeding the mobile brine fraction (Φ_{eff}/Φ_{tot}) here, as shown by the light green signature in Fig. 6, indicating that the conventional saturation model is again not leading to fully consistent results assuming displacement alone. In the upper part, the Σ and TPHI logs slightly decrease after the fourth repeat in the upper sandstone layer, whereas in the lower part a slight increase can be observed. The shape of the saturation profile is changing accordingly, with an increase of S_{CO2} in the upper and a decrease in the lower part of the upper sandstone layer.

In the lower sandstone layer, only the Σ and TPHI logs of the second repeat show a significant decrease compared to the baseline log. This is interpreted as an effect related to the displacement of brine by CO_2 within the annulus, which is related to a temporary drop of the brine level within the well during this repeat run. A temporary change of saturation within a larger part of the reservoir does not seem plausible from a hydrodynamic point of view, considering the relatively uniform injection regime during this time. The decrease of Σ and TPHI within the caprock section immediately above the reservoir interval is also interpreted as a result of accumulation of CO_2 within the annulus, similar to the conditions described for Ktzi 201 (see above). In Ktzi 200, the effect is nevertheless limited to a much smaller depth interval, as the bottom of the cement is located only a few meters above the reservoir section (see Fig. 6, panel ii).

5.1.3. Observation well Ktzi 202

The repeat Σ and TPHI logs are decreased relative to the baseline until repeat five down to a depth of approx. 649 m, which also corresponds to the position of the brine levels during the respective logging runs (Fig. 7). Afterwards, the brine level is rising to a depth of 634.34 m, and Σ and TPHI again return to their baseline values below this depth for repeat six. The observed reductions in Σ and TPHI below this depth are therefore attributed to displacement of brine by CO_2 within the annulus. In the interval between 637 and 641 m, where the repeat Σ and TPHI logs increasingly overlap with the baseline log, the annulus is most likely blocked by a formation collapse, and could therefore not be invaded by CO_2.

In the main reservoir sandstone layer, a continuous decrease of Σ and TPHI is visible until repeat four in the upper part above 631.6 m, where below this depth all repeats overlap. Therefore, the interval below the pivot point at 631.6 m is also assumed to be influenced by CO_2 within the annulus and CO_2 saturation profiles have therefore been derived for the upper part (627.55 - 631.6 m) of the reservoir sandstone layer only. The calculated S_{CO2} increases from an average value of 35 % during the second repeat to 57 % for repeat four. For the subsequent repeats, S_{CO2} as well as the shape of the CO_2 saturation profile roughly remain unchanged. In this case, the calculated CO_2 saturations are smaller than the mobile brine fraction (Φ_{eff}/Φ_{tot}), showing that the conventional saturation model is sufficient to describe the measured data.

5.2. Extended saturation model

In the following text the application of the extended saturation model for the injection well Ktzi 201 is discussed. In addition to considering the effects of evaporation and salt precipitation, the synthetic Σ and TPHI baseline logs are used, in order to account for the low-salinity KCl-preflush.

As indicated by temperature anomalies observed during distributed temperature sensing monitoring, the KCl-preflush was mainly injected into the upper and lower sandstone layers. The total KCl-preflush volume is 30.5 m³, with a salinity of 60 ppk KCl, which corresponds to a Σ value of 39.5 cu (p 97 in Baumann, 2013).

For calculation of the synthetic baseline logs it is assumed that the total KCl-preflush volume is injected homogeneously over the entire depth range, and that the mobile brine in Φ_{eff} is completely displaced. Afterwards, a diffusion driven salinity equilibration between the low salinity KCl-preflush brine (Φ_{eff}) and the high salinity formation brine (Φ_{irr}) is assumed. Based on these assumptions, first a synthetic Σ flush brine log and afterwards the synthetic Σ and TPHI flush baseline logs (SIGM_b-fl and TPHI_b-fl) have been calculated (pp 96-100 in Baumann, 2013).

According to the reduced salinity, the SIGM_b-fl log has smaller values than the measured baseline log. In effect, the repeat Σ logs are greater than the SIGM_b-fl log in the upper and lower part of the upper sandstone layer (Fig. 8). The depth range in the lower sandstone layer, with repeat Σ logs greater than the SIGM_b-fl log, increases from the second to all subsequent repeats. Accordingly, using the SIGM_b-fl log, the case $\Sigma_r > \Sigma_b$ applies in more depth intervals than using the original Σ baseline log. The TPHI_b-fl log is slightly greater than the original TPHI baseline log, because the HI values of the pre-flush brine are slightly higher than the original formation brine value. However, in contrast to the baseline Σ logs, the difference is much smaller, because HI is less affected by changing salinities than Σ.

5.2.1. Case $\Sigma_R \leq \Sigma_B$:

In the middle part of the upper sandstone layer and the upper part of the lower sandstone layer the case $\Sigma_R \leq \Sigma_B$ applies. The porosity adjustment is applied, indicated by the white dashed curve in Fig. 6, in order to get the best fit between the measured and modeled data (see Section 4.2.1).

The depth intervals where no residual brine remains, and thus only CO_2 and halite are present, are the dry-out regions. This applies in the middle part of the upper sandstone layer for all repeats, as well as in the upper part of the lower sandstone layer, except for repeat six. Especially in the upper sandstone layer, the S_{NaCl} values are maximal at the upper and lower edges and decrease towards the centers of the dry-out regions. The maximum S_{NaCl} value in the dry out regions is 1.2 % and occurs during the fourth repeat.

5.2.2. Case $\Sigma_R > \Sigma_B$:

The case $\Sigma_R > \Sigma_B$ applies at the upper and lower edges of the upper sandstone layer, and in most parts the lower sandstone layer. In the intervals with positive TPHI values, the CO_2 saturation is calculated based on TPHI (see Section 4.2.2). This applies to the intervals in the lower sandstone layer below the corresponding brine levels, including the prominent Σ peaks above the baseline level during repeats four and five, as well as up to 648.6 m for the second repeat. Above these depth intervals, $S_{CO2\text{-}eff}$ is set to one and $S_{CO2\text{-}irr}$ is set to zero for the $\Sigma_R > \Sigma_B$ case (see Section 4.2.2). In contrast to the first case $\Sigma_R < \Sigma_B$, the effective porosity did not need to be adjusted in order to get the best fit model.

A maximum S_{NaCl} value of 14.1 % is calculated for zone of the prominent Σ peak during the fourth repeat in the middle part of the lower sandstone layer. During repeat five, the extent of the calculated halite-bearing zone is decreasing, corresponding to the decrease of the Σ peak. For the sixth repeat, halite saturation is finally reduced to zero again within this interval, which is also correlating with a rise of the brine level above this depth.

Compared to the results from the conventional saturation model, the shape of the saturation profiles is more variable, and S_{CO2} is generally higher, especially in the dry-out regions, as well as within the zone with increased Σ above the baseline value.

6. Discussion

The derived saturation profiles for the observation well Ktzi 202, which is further away from the injection well, show that only mobile brine displacement has occurred at this position (Fig. 7). The CO_2 saturation gradually increases from the second to the fourth repeat and remains rather constant afterwards. Compared to Ktzi 201 and Ktzi 200, the CO_2 saturation is smallest in Ktzi 202, with average values below 60 %.

In the observation well Ktzi 200, which is closer to the injection well, CO_2 saturation is increasing faster, and reaches maximum averages slightly above 60 % during the fourth and fifth repeat. A change of the saturation profile shape, with increasing CO_2 saturation at the top, and decreasing saturation at the bottom of the main storage horizon (Fig. 6) is observed for the fifth and sixth repeats. With respect to the injection regime, which is characterized by lower injection rates and longer shut-in periods during this time, this indicates a transition from predominantly advection-driven lateral spreading to a more gravity-driven rise of the CO_2 plume.

As can be expected, the largest CO_2 saturations with average values up to 68 % are determined in the injection well Ktzi 201. Locally, saturations of up to 100 % occur in the middle part of the upper sandstone and the upper part of the lower sandstone, and are already reached early on (Fig. 5). Average CO_2 saturations of up to 21 % are also occurring in the sand- and siltstone interval below the main injection interval during repeat two and three. The temporary invasion of CO_2 into this interval is also confirmed by independent information from borehole temperature data acquired using the permanently installed distributed temperature sensing cables. Temperature anomalies related to the injection process can be observed during the initial injection phase until March 2010. During this time the CO_2 injection zone has the greatest vertical extent, corresponding to the period with highest injection rates. After repeat three, the CO_2 saturation in the lower intervals is decreasing as a result

14

of the reduced injection rate. A general decrease of CO_2 saturation during repeat six applies to all wells but is most obvious in Ktzi 201, and corresponds with the six-month shut-in period preceding this measurement.

There are clear indications that in addition to displacement, evaporation and precipitation processes have occurred in Ktzi 201. In the middle of the upper sandstone as well as at the upper edge of the lower sandstone layer, the CO_2 saturation calculated from the standard displacement model significantly exceeds the mobile brine fraction (Fig. 5). Using the extended saturation model, these zones result in dry-out regions where only CO_2 and halite with saturations up to 1.4 % exist (Fig. 8). The positions of the dry-out regions also correspond to the locations where the largest temperature anomalies were observed during the KCl-preflush. This validates that these depth intervals have the highest injectivities, as can be expected for the dry-out regions. The distribution of the halite saturation in the dry-out regions, with higher values at the edges and lower values in the centre, can be explained with the presence of large capillary forces leading to influx of additional brine at the edges.

The prominent peaks of the Σ logs between 645 m and 646 m during repeat four and five are best explained by the presence of additional salt load. The measurement data can only be explained by the extended saturation model, where the greatest halite saturations are calculated around these depths, with values up to 14.1 %. They are located in the vicinity of the brine levels, where large capillary forces occur. Due to changing brine levels, which are associated with changes of the injection regime, precipitated halite goes back into solution.

The lowest halite saturations are derived in the dry-out regions corresponding to low repeat Σ values, whereas the highest halite saturations are in the vicinity of the brine levels, corresponding to high repeat Σ values. Since the precision of the RST tool is inversely proportional to Σ (Kimminau und Plasek, 1992), a greater accuracy can be expected for the low rather than for the high derived halite saturations.

A number of different numerical simulation studies considering evaporation/precipitation effects have been performed for the Ketzin site (Hurter et al., 2007; Muller et al., 2009; Zeidouni et al., 2009). The used models differ in their underlying assumptions or complexity regarding capillary or gravitational effects, as well as regarding geometry and discretization. The calculated dry-out radii range between 3.8 and 13 m, and maximum halite saturations range between 3 % (Zeidouni et al., 2009a) and 80 % (Hurter et al., 2007). Muller et al. (2009) arrive at maximum halite saturations between 3 % and 16.6 %, respectively if the KCl-preflush is considered or not, which is in good agreement with the results of the extended PNG saturation model presented here.

In Ktzi 200 the calculated CO_2 saturations indicate that evaporation may have also occurred in some depth intervals of the upper sandstone layer. This is nevertheless not in accordance with the above mentioned results of numerical modeling studies, which predict a much smaller lateral extent of the dry-out zone around the injection well. On the one hand, these modeling studies are based on simplifications and do not sufficiently account for the lithological heterogeneities of the reservoir section, or the changing injection rate. Preferential flow paths could exist, leading to a larger extent of the dry-out zone than numerically predicted. On the other hand, larger uncertainties have to be expected for the porosity data of Ktzi 200, because this well was characterized by a less comprehensive open hole logging program than Ktzi 201 (Norden et al., 2010). Thus an underestimation of Φ_{eff} could also account for the discrepancy with the PNG monitoring data. A detailed description of results of the extended saturation model for Ktzi 200 was therefore not included within this paper, but can be found in Baumann (2013).

It was found that strong effects on the PNG data were caused by fluid changes in the uncemented sections of the well annuli. Using the open-hole logging porosity data and the air correction as an input to the RST processing algorithm for the repeat logging runs could partially bypass the influence on the measured formation Σ values. But since the RST processing algorithm assumes cemented annuli, a negative effect on the accuracy cannot be excluded. For the injection well Ktzi 201, the greatest uncertainty results from the baseline logging data, which was acquired before the KCl preflush. Under the given conditions, the presented results for the extended saturation model represent the best possible synthesis of the existing open- and cased hole logging data, accounting for all available information on borehole and fluid conditions including the KCl-preflush before start of injection.

At Ketzin, no obvious loss of injectivity which could be linked to the salt precipitations described here has been observed. With respect to the total mass of CO_2 injected they are likely a near-well phenomenon and only occur locally, with no strong effect on fluid pathways within the reservoir overall. If substantially higher amounts of CO_2 would be involved, salt precipitation could nevertheless severely influence injectivity, as experiences from gas production and storage have shown.

7. Conclusions

Based on the PNG monitoring performed within the injection period between June 2008 and August 2013, saturation profiles are determined for the injection (Ktzi 201) and two observation wells (Ktzi 200 and Ktzi 202) at the Ketzin site. The spatio-temporal evolution of the saturation conditions can be summarized as follows:

- Maximum CO_2 saturation at Ktzi 201: 68 % (average) - 100 % (local)
- Decrease of CO_2 saturation towards Ktzi 200 (> 60 %), and Ktzi 202 (< 60 %)
- Greatest vertical extent of CO_2 plume during time with highest injection rates
- Transition from predominantly advection-driven lateral spreading to a more gravity-driven rise of the CO_2 plume during time with lower injection rates and longer shut-in periods

The CO_2 saturation calculated from the standard displacement model partly exceeds the mobile brine fraction significantly, especially in Ktzi 201. This indicates that in addition to displacement, evaporation has occurred. The prominent peaks of the Σ logs between 645 m and 646 m during repeat four and five are best explained by the presence of an additional salt load which has precipitated in the pore space. In order to account for the combined effects of displacement, evaporation, and salt precipitation, a new extended saturation model has been developed. The results indicate that halite saturations up to 1.4 % occur within dry-out regions, where only CO_2 and halite are present within the pore space. The greatest halite saturations up to 14.1 % occur in the vicinity of the brine levels. In general, the halite saturation distribution in the injection well seems to be controlled by the combined effect of changes in the injection regime, lithological heterogeneities, and capillary effects.

The adverse effects of fluid changes in the uncemented sections of the well annuli on the PNG repeat logging data could partially be compensated by using the open-hole logging porosity data and the air correction as an input to the RST processing algorithm. In order to avoid such effects, either wells should be completed with fully cemented annuli, or enhanced tool calibration for related borehole

conditions would be required. Baseline PNG data should be acquired under conditions as close as possible to the repeat logging runs.

PNG logging, in combination with the presented extended saturation model, is suitable to depict the saturation conditions under conditions given within this study. For projects involving larger injection volumes, salt precipitation could be monitored using this method at an early stage before leading to a possible adverse impairment of the flow paths around an injection well.

SI conversion:

1 inch = 0.0254 m

1 lb/ft = 1.4882 kg/m

1 cu = $1*10^{-3}$ cm^{-1} = $1*10^{-1}$ m^{-1}

1 g/cm³ = 1000 kg/m³

1 cm²/g = 0.1 m²/kg

References:

Afeefy, H. Y., Liebman, J. F., Stein, S. E., 2005. Neutral thermochemical Data. In: NIST Chemistry WebBook, NIST Standard Reference Database Number 69, (Eds. P. J. Linstrom and W. G. Mallard). National Institute of Standards and Technology, Gaithersburg MD, 20899, (http://webbook.nist.gov).

Baumann, G., 2013. Determination of displacement and evaporation/precipitation processes via Pulsed Neutron-Gamma (PNG) monitoring for CO_2 storage operations. Ph.D. Thesis, Technical University of Berlin, Germany.

Baumann, G., Henninges, J., 2012. Sensitivity study of pulsed neutron-gamma saturation monitoring at the Altmark site in the context of CO_2 storage, Environmental Earth Sciences 67 (2), 463-471, doi: 10.1007/s12665-012-1708-x.

Bergmann, P., Schmidt-Hattenberger, C., Kiessling, D., Rücker, C., Labitzke, T., Henninges, J., Baumann, G., Schütt, H., 2012. Surface-downhole electrical resistivity tomography applied to monitoring of CO_2 storage at Ketzin, Germany. Geophysics 77 (6), B253-B267. doi: 10.1190/geo2011-0515.1.

Ellis, D. V., Faum, C., Galford, J. E., Scott, H., 1987. The effect of formation absorption on the thermal neutron porosity measurement. In: SPE Annual Technical Conference and Exhibition, 27-30 September 1987, Dallas, TX, pp. 16. doi: 10.2118/16814-MS.

Förster, A., Schöner, R., Förster, H.-J., Norden, B., Blaschke, A.-W., Luckert, J., Beutler, G., Gaupp, R., Rhede, D, 2010. Reservoir characterization of a CO_2 storage aquifer: the Upper Triassic Stuttgart Formation in the Northeast German Basin. Marine and Petroleum Geology 27 (10), 2156-2172.

Giese, R., Henninges, J., Lüth, S., Morozova, D., Schmidt-Hattenberger, C., Würdemann, H., Zimmer, M., Cosma, C., Juhlin, C., CO_2SINK Group, 2009. Monitoring at the CO_2SINK site: a concept integrating geophysics, geochemistry and microbiology, Energy Procedia 1 (1), 2251-2259.

Hurter, S., Labregere, D., Berge, J., 2007. Simulations for CO_2 Injection Projects With Compositional Simulator. Society of Petroleum Engineers, pp. 8. doi: 10.2118/108540-MS.

Ivanova, A., Kashubin, A., Juhonjuntti, N., Kummerow, J., Henninges, J., Juhlin, C., Lüth, S., Ivandic, M., 2012. Monitoring and volumetric estimation of injected CO_2 using 4D seismic, petrophysical data, core measurements and well logging: A case study at Ketzin, Germany. Geophysical Prospecting 60, 957-973. doi: 10.1111/j.1365-2478.2012.01045.x.

Kimminau, S., Plasek, R., 1992. The design of pulsed neutron reservoir monitoring programs. SPE Formation Evaluation 7 (1), 93-98. doi: 10.2118/20589-PA.

Kleinitz, W., Dietzsch, G., Köhler, M., 2003. Halite scale formation in gas-producing wells. Chemical Engineering Research and Design 81, 352-358.

Kummerow, J., Spangenberg, E., 2011. Experimental evaluation of the impact of CO_2-SO_2-brine reservoir rock interactions on petrophysical properties: a case study from the Ketzin test site, Germany. Geochemistry Geophysics Geosystems 12 (5), Q05010. DOI: 10.1029/2010GC003469

Martens, S., Kempka, T., Liebscher, A., Lüth, S., Möller, F., Myrttinen, A., Norden, B., Schmidt-Hattenberger, C., Zimmer, M., Kühn, M., The Ketzin Group, 2012. Europe's longest-operating on-shore CO_2 storage site at Ketzin, Germany: a progress report after three years of injection. Environ. Earth Sci. 67, 323-334.

Martens, S., Liebscher, A., Möller, F., Henninges, J., Kempka, T., Lüth, S., Norden, B., Prevedel, B., Szizybalski, A., Zimmer, M., Kühn, M., the Ketzin Group, 2013. CO_2 storage at the Ketzin pilot site, Germany: Fourth year of injection, monitoring, modelling and verification. Energy Procedia 37, 6434-6443.

Möller, F., Liebscher, A., Martens, S., Schmidt-Hattenberger, C., Kühn, M., 2012. Yearly Operational Datasets of the CO_2 Storage Pilot Site Ketzin, Germany. Helmholtz Centre Potsdam GFZ German Research Centre for Geosciences, Scientific Technical Report STR12/06 - Data, pp. 14. doi: 10.2312/GFZ.b103-12066.

Müller, N., Ramakrishnan, T., Boyd, A., Sakurai, S., 2007. Time-lapse carbon dioxide monitoring with pulsed neutron logging. International Journal of Greenhouse Gas Control 1 (4), 456-472. doi: 10.1016/S1750-5836(07)00071-0.

Muller, N., Qi, R., Mackie, E., Pruess, K., Blunt, M. J., 2009. CO_2 injection impairment due to halite precipitation. Energy Procedia 1 (1), 3507-3514.

Murray, D., Wang, Y. X., Horie, T., Yoshimura, T., Mito, S., 2010. CO_2 sequestration monitoring in a low formation water salinity reservoir. In: International Oil and Gas Conference and Exhibition in China, 8-10 June 2010, Beijing, China, SPE Society of Petroleum Engineers. doi: 10.2118/130773-MS.

Norden, B., Förster, A., Vu-Hoang, D., Marcelis, F., Springer, N., Nir, I. L., 2010. Lithological and petrophysical core-log interpretation in CO_2SINK, the European CO_2 onshore research storage and verification project. SPE Reservoir Evaluation & Engineering 13 (2), 179-192. doi: 10.2118/115247-PA.

Plasek, R., Adolph, R., Stoller, C., Willis, D., Bordon, E., Portal, M., 1995. Improved pulsed neutron capture logging with slim carbon-oxygen tools: methodology. In: SPE Annual Technical Conference and Exhibition, 22-25 October 1995, Dallas, TX, pp. 15. doi: 10.2118/30598-MS.

Prevedel, B., Wohlgemuth, L., Henninges, J., Krüger, K., Norden, B., Förster, A., The CO_2SINK Drilling Group, 2008. The CO_2SINK boreholes for geological storage testing. Scientific Drilling 6, 32-37.

Pruess, K. Müller, N., 2009. Formation dry-out from CO_2 injection into saline aquifers: 1. Effects of solids precipitation and their mitigation. Water Resources Research 45 (3), pp. 11. doi: 10.1029/2008WR007101.

Rowe, A. M., Chou, J. C. S., 1970. Pressure-volume-temperature-concentration relation of aqueous sodium chloride solutions. Journal of Chemical and Engineering Data 15 (1), 61-66. doi: 10.1021/je60044a016.

Potter, R. W., Babcock, R. S., Brown, D. L., 1977. A new method for determining the solubility of salts in aqueous solutions at elevated temperatures. J. Research U. S. Geol. Surv. 5, 389-395.

Sakurai, S., Hovorka, S., Ramakrishnan, T. S., Boyd, A., Mueller, N., 2005. Monitoring saturation changes for CO_2 Sequestration: petrophysical support of the Frio Brine pilot experiment. SPWLA, 46th Annual Logging Symposium, pp. 16.

Sears, V. F., 1992. Neutron scattering lengths and cross sections, Neutron News 3 (3), 29-37.

Serra, O., 1984. Fundamentals of well-log interpretation, vol. 1. Elsevier Science Publishers B. V.

Spycher, N., Pruess, K., Ennis-King, J., 2003. CO_2-H_2O mixtures in the geological sequestration of CO_2. I. Assessment and calculation of mutual solubilities from 12 to 100°C and up to 600 bar. Geochimica et Cosmochimica Acta 67 (16), 3015-3031. doi: 10.1016/S0016-7037(03)00273-4.

Spycher, N. Pruess, K., 2005. CO_2-H_2O mixtures in the geological sequestration of CO_2. II. Partitioning in chloride brines at 12 - 100°C and up to 600 bar. Geochimica et Cosmochimica Acta 69 (13), 3309-3320, doi: 10.1016/j.gca.2005.01.015.

Tesmer, M. Möller, P., Wieland, S., Jahnke, C., Voigt, H., Pekdeger, A., 2007. Deep reaching fluid flow in the North East German Basin: origin and processes of groundwater salinisation. Hydrogeology Journal 15, 1291-1306. doi: 10.1007/s10040-007-0176-y.

Würdemann, H., Möller, F., Kühn, M., Heidug, W., Christensen, N. P., Borm, G., Schilling, F. R., The CO_2SINK Group, 2010. CO_2SINK - From site characterisation and risk assessment to monitoring and verification: one year of operational experience with the field laboratory for CO_2 storage at Ketzin, Germany. International Journal of Greenhouse Gas Control 4 (6), 938-951. doi: 10.1016/j.ijggc.2010.08.010.

Xue, Z., Tanase, D., Watanabe, J., 2006. Estimation of CO_2 saturation from time-lapse CO_2 well logging in an onshore aquifer, Nagaoka, Japan. Exploration Geophysics 37 (1), 19-29, doi: 10.1071/EG06019.

Zeidouni, M., Pooladi-Darvish, M., Keith, D., 2009. Analytical solution to evaluate salt precipitation during CO_2 injection in saline aquifers. International Journal of Greenhouse Gas Control 3 (5), 600-611. doi: 10.1016/j.ijggc.2009.04.004.

Zimmer, M., Erzinger, J., Kujawa, C., 2011. The gas membrane sensor (GMS): a new method for gas measurements in deep boreholes applied at the CO_2SINK site. International Journal of Greenhouse Gas Control 5 (4), 995-1001. doi: 10.1016/j.ijggc.2010.11.007.

Figures

Fig. 1: Aerial view of the Ketzin site during drilling of observation well Ktzi 203 in September 2012 (Martens et al., 2013)
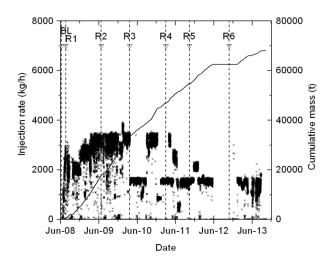

Fig. 2: Times of PNG baseline (BL) and repeat (R) logging runs, together with CO_2 injection data (after Möller et al., 2012) from June 2008 until the end of injection in August 2013.
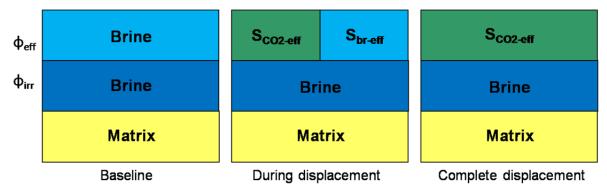
Fig. 3: **Conventional displacement saturation model** *Baseline:* before CO_2 injection the formation is fully brine saturated. *During displacement:* the mobile brine (Φ_{eff}) is displaced by CO_2 and $S_{CO2\text{-}eff}$ (saturation value referred to Φ_{eff} only) is less than one during displacement. *Complete displacement:* after complete displacement, $S_{CO2\text{-}eff}$ is equal to one. The immobile brine (Φ_{irr}) is unaffected by the displacement process.
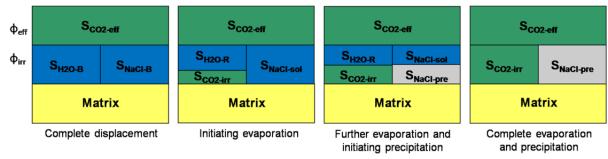
Fig. 4: **Extended displacement and evaporation/precipitation saturation model** *Complete displacement:* the mobile brine (Φ_{eff}) is completely displaced and $S_{CO2\text{-}eff}$ is equal to one. *Initiating evaporation:* the immobile brine (Φ_{irr}) evaporation initiates. *Further evaporation, initiating precipitation:* the NaCl solubility limit is reached and precipitation ($S_{NaCl\text{-}pre}$) initiates. *Complete evaporation and precipiation:* $S_{CO2\text{-}irr}$ is reduced by the occupied precipitated halite fraction. $S_{NaCl\text{-}pre}$ is equal to the initial NaCl saturation ($S_{NaCl\text{-}B}$) in Φ_{irr}.

Ktzi 201

Depth	i	ii	iii	iv	v	vi	vii	viii	ix	x
1:250	L-201	C-201	201_TPHI	201_TPHI_b	201_SIGM_b	S_CO2_r2	S_CO2_r3	S_CO2_r4	S_CO2_r5	S_CO2_r6
m		GR	0 V/V 0.4 201_EPHI	-0.3 V/V 0.6 201_TPHI_r2	70 cu 10 201_SIGM_r2	S_br_r2	S_br_r3	S_br_r4	S_br_r5	S_br_r6
			0 V/V 0.4 201_TPHI_r3	-0.3 V/V 0.6 201_SIGM_r3	70 cu 10					
				-0.3 V/V 0.6 201_TPHI_r4	70 cu 10 201_SIGM_r4	0 V/V 1	0 V/V 1	0 V/V 1	0 V/V 1	0 V/V 1
				-0.3 V/V 0.6 201_TPHI_r5	70 cu 10 201_SIGM_r5					
				-0.3 V/V 0.6 201_TPHI_r6	70 cu 10 201_SIGM_r6					
				-0.3 V/V 0.6	70 cu 10					

Legend:
- Sandstone (ss)
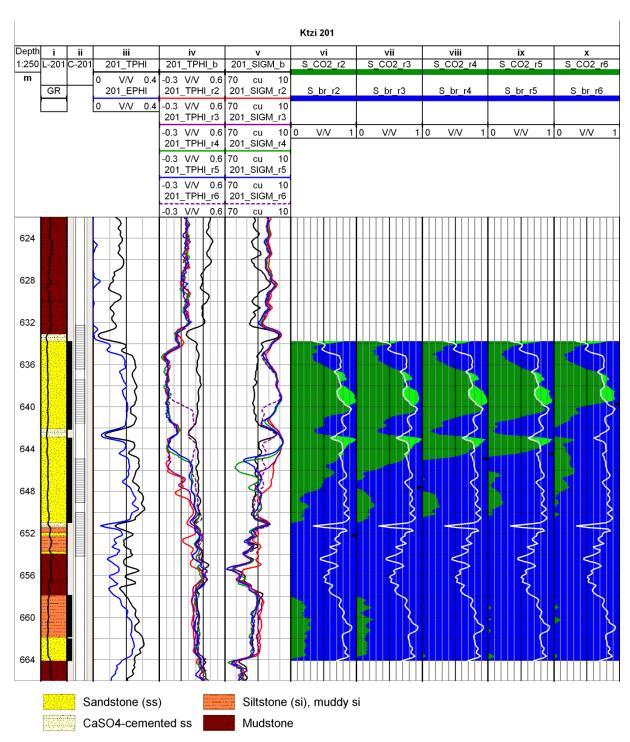- Siltstone (si), muddy si
- CaSO4-cemented ss
- Mudstone

Fig. 5: Ktzi 201 saturation profiles (vi to x) as fractions of Φ_{tot} based on the displacement saturation model and the original brine salinity (displacement conform CO_2 in green, apparent CO_2 in light green and brine in blue). The white log for each repeat run separates the mobile from the immobile brine. The brine levels for each repeat run are marked with a black bar on the right side of the saturation profiles. Lithology (i) after Förster et al. (2010), well completion (ii), total (TPHI) and effective (EPHI) porosity logs (iii) after Norden et al. (2010), neutron porosity TPHI (iv) and Σ (v) logs from the PNG baseline and five repeat runs.

Fig. 6: Ktzi 200 saturation profiles (tracks vi to xi) as fractions of Φ_{tot} based on the displacement saturation model (displacement conform CO_2 in green, apparent CO_2 in light green and brine in blue). The white log for each repeat run separates the mobile from the immobile brine. The brine levels for each repeat run are marked with a black bar on the right side of the saturation profiles. Lithology (i) after Förster et al. (2010), well completion (ii), total (TPHI) and effective (EPHI) porosity logs (iii) after Norden et al. (2010), neutron porosity TPHI (iv) and Σ (v) logs from the PNG baseline and six repeat runs.
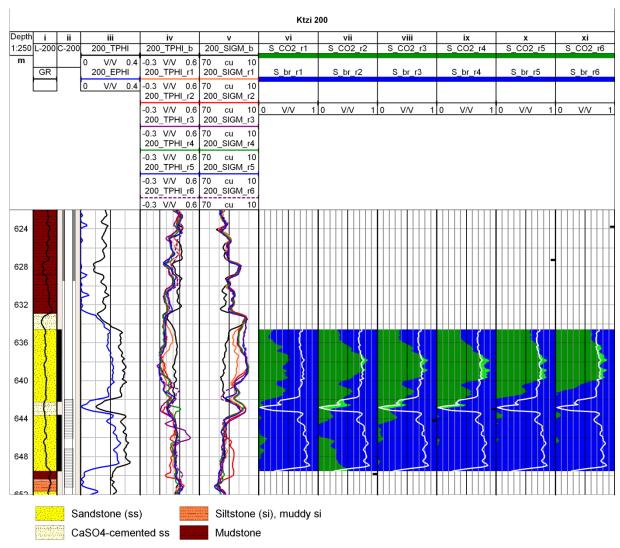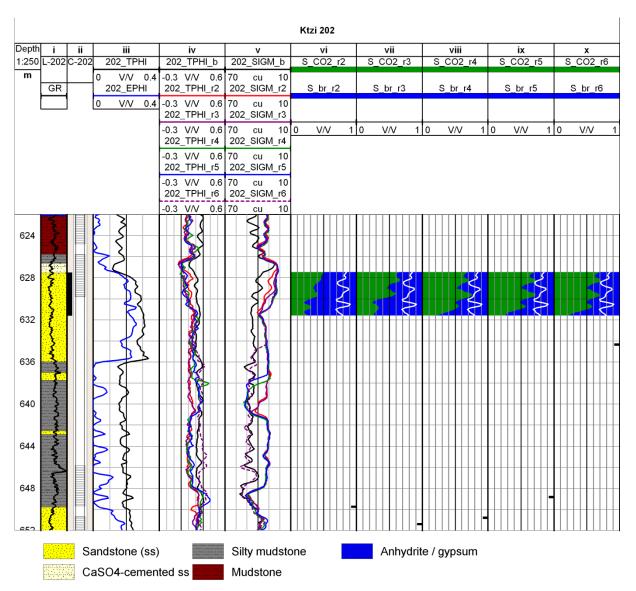
Fig. 7: Ktzi 202 saturation profiles (tracks vi to x) as fractions of Φ_{tot} based on the displacement saturation model (displacement conform CO_2 in green, apparent CO_2 in light green and brine in blue). The white log for each repeat run separates the mobile from the immobile brine. The brine levels for each repeat run are marked with a black bar on the right side of the saturation profiles. Lithology (i) after Förster et al. (2010), well completion (ii), total (TPHI) and effective (EPHI) porosity logs (iii) after Norden et al. (2010), neutron porosity TPHI (iv) and Σ (v) logs from the PNG baseline and five repeat runs.
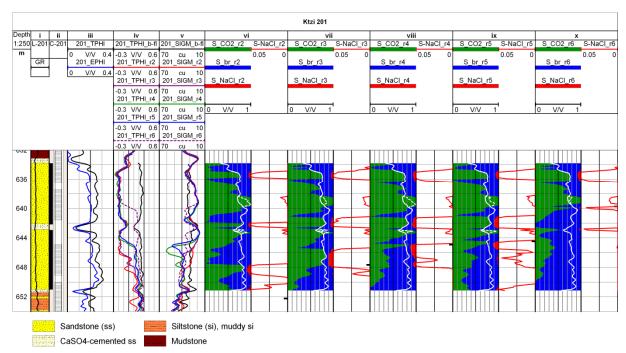
Fig. 8: Ktzi 201 saturation profiles (vi to x) as fractions of Φ_{tot} (CO_2 in green, brine in blue, halite in red) including halite saturations in a smaller scale based on the extended saturation model and the flush brine salinity with porosity adjustment. The white solid log for each repeat run separates the mobile from the immobile brine. The white dotted logs show the adjustment of the affected porosities. The brine levels for each repeat run are marked with a black bar on the right side of the saturation profiles. Lithology (i) after Förster et al. (2010), well completion (ii), total (TPHI) and effective (EPHI) porosity logs (iii) after Norden et al. (2010), neutron porosity TPHI (iv) and Σ (v) logs from the PNG flush baseline and five repeat runs.

Tables

Table 1: The calculated fluid Σ values under Ketzin reservoir conditions (35 °C, 7.5 MPa).

Σ_{NaCl-c} [cu]	Σ_{H2O-c} [cu]	Σ_{br} [cu]	Σ_{CO2} [cu]
77.15	22.43	97.58	0.014

Table 2: The dates on which the RST runs were carried out in the wells Ktzi 200, Ktzi 201 and Ktzi 202, and the predominant well fluids.

Run	Well fluid	Ktzi 200	Ktzi 201	Ktzi 202
b	brine	10.06.08	09.06.08	09.06.08
r1	brine	21.07.08	-	-
r2	CO_2	25.06.09	24.06.09	26.06.09
r3	CO_2	22.03.10	23.03.10	22.03.10
r4	CO_2	01.03.11	02.03.11	03.03.11
r5	CO_2	13.10.11	14.10.11	12.10.11
r6	CO_2	24.10.12	26.10.12	25.10.12

26

Table 3: Brine levels below ground level for the repeat runs in Ktzi 200, Ktzi 201 and Ktzi 202. The elevation of the ground surface is similar for all wells within 0.1 m.

Run	Ktzi 200	Ktzi 201	Ktzi 202
	[m]	[m]	[m]
r1	206.35	-	-
r2	649.83	652.22	649.74
r3	644.19	647.65	651.41
r4	642.98	644.90	650.80
r5	627.28	644.44	648.82
r6	623.77	639.72	634.34

Table 4: The used abbreviations for the conventional and extended saturation model as well asl for the calculation of the fluid Σ values

Mnemonic	Description	Unit
c_{H2O}	water concentration in brine	g/l
$c_{NaCl-eq}$	NaCl-equivalent concentration in brine	g/l
S_{br}	total brine saturation	-
S_{br-eff}	brine saturation in Φ_{eff}	-
S_{br-irr}	irreducible brine saturation	-
S_{CO2}	total CO_2 saturation	-
$S_{CO2-eff}$	CO_2 saturation in Φ_{eff}	-
$S_{CO2-irr}$	CO_2 saturation in Φ_{irr}	-
$S_{H2O-lim}$	water volume fraction in NaCl saturated brine	-
S_{H2O-B}	initial water volume fraction in brine	-
S_{H2O-R}	remaining water saturation in Φ_{irr}	-
$S_{NaCl-lim}$	NaCl volume fraction in NaCl saturated brine	-
$S_{NaCl-pre}$	precipitated halite saturation in Φ_{irr}	-
$S_{NaCl-sol}$	dissolved NaCl saturation in Φ_{irr}	-
S_{NaCl-B}	initial NaCl volume fraction in brine	-
ρ_{br}	brine density	g/cm³
ρ_{H2O-br}	auxiliary water density in brine	g/cm³
ρ_{NaCl}	Halite density	g/cm³
σ_{m-NaCl}	NaCl mass-normalized microscopic capture cross section	cm²/g
σ_{m-H2O}	water mass-normalized microscopic capture cross section	cm²/g
Φ_{eff}	mobile porosity fraction	-
Φ_{irr}	immobile porosity fraction	-
Φ_{tot}	total porosity	-
Σ_{br}	Σ brine	cu
Σ_{br-lim}	Σ value for NaCl saturated brine	cu
Σ_{ma}	Σ matrix	cu
Σ_{CO2}	Σ CO_2	cu
Σ_B	baseline Σ	cu
Σ_{B-eff}	baseline Σ Φ_{eff} fraction	cu
Σ_{B-irr}	baseline Σ Φ_{irr} fraction	cu
Σ_{B-ma}	baseline Σ matrix fraction	cu
Σ_{H2O-br}	Σ water in brine	cu
Σ_{H2O-c}	Σ water fraction in brine	cu
Σ_{NaCl}	Σ halite	cu
Σ_{NaCl-c}	Σ NaCl fraction in brine	cu
Σ_R	Repeat Σ	cu
Σ_{R-eff}	repeat Σ Φ_{eff} fraction	cu
Σ_{R-irr}	repeat Σ Φ_{irr} fraction	cu
Σ_{R-ma}	repeat Σ matrix fraction	cu

Table 5: Average CO_2 saturations calculated with the standard displacement (Disp.) and the extended (Ext.) saturation model for the six PNG repeat logging runs. The extent of the averaging intervals is marked with black bars in Figs. 5-8.

Well	Interval		Top	Bottom	Thickness	Phi	S_{r1}	S_{r2}	S_{r3}	S_{r4}	S_{r5}	S_{r6}
			(m)	(m)	(m)	(%)	(%)	(%)	(%)	(%)	(%)	(%)
201	1	Disp.	633.75	642.09	8.34	23.5	–	67	63	61	60	50
		Ext.					–	57	64	68	65	55
	2	Disp.	642.87	650.99	8.12	25.9	–	50	37	25	23	15
		Ext.					–	50	56	39	45	21
	3		657.89	661.85	3.96	26.3	–	21	14	0	1	2
	4		661.85	664.11	2.26	27.2	–	18	12	1	2	1
200	1		634.58	642.24	7.66	27.5	36	55	58	61	62	58
	2		643.66	649.49	5.83	29.6	3	22	6	1	1	1
202	1		627.55	631.6	4.05	28.2	–	35	46	57	57	56